Unified Active Damping Control Algorithm of Inverter for LCL Resonance and Mechanical Torsional Vibration Suppression

Liu, Xiong; Qi, Yangxiao; Tang, Yi; Guan, Yuanpeng; Wang, Peng; Blaabjerg, Frede

Published in:
I E E E Transactions on Industrial Electronics

DOI (link to publication from Publisher):
10.1109/TIE.2021.3095796

Publication date:
2022

Document Version
Accepted author manuscript, peer reviewed version

Unified Active Damping Control Algorithm of Inverter for LCL Resonance and Mechanical Torsional Vibration Suppression

Xiong Liu, *Senior Member*, *IEEE*, Yang Qi, *Student Member IEEE*, Yi Tang, Senior *Member*, *IEEE*, Yuanpeng Guan, Peng Wang, *Fellow*, *IEEE*, and Frede Blaabjerg, *Fellow*, *IEEE*

***Abstract*—In the electrical engineering field, there are two types of system which can potentially generate resonance under excitation, one is the electrical system with inductor and capacitor, the other is the mechanical system with spring-mass characteristic. A lot of research on active damping control algorithms for grid-connected inverters with LCL filter and inverter-driven machine with multi-rotating masses have been demonstrated. However, research works for these two systems were carried out independently and there is a lack of systematic comparison for modelling and control between these two systems. This paper will unify the mathematical models and active damping control algorithms for these two systems. It is found that the mathematical models and control structures are fundamentally the same. The existing or future potential active damping control algorithms used in electrical system can be applied in mechanical system and vice versa to avoid reinventing the wheel. Parameter sensitivity analysis for controller and feedback gains was performed for electrical systems in the discrete z-domain. For mechanical systems, it is found that a substantial electromagnetic torque overshoot was introduced when applying the active damping control and it was analyzed quantitatively with various damping coefficients to guide the inverter design. Finally, experimental tests were done to verify the findings.**

***Index Terms*—Active Damping, LCL filter, Torsional Vibration, Multi-rotating Mass, Torque Overshoot.**

I. Introduction

GRID-connected inverters have been widely used for integrating various distributed generations in recent years. In order to decrease grid-side current harmonics with reduced filter size, *LCL* filters are commonly used to replace the *L* filter [1]–[3]. However, *LCL* filters can cause stability issues due to the inherent resonance characteristic. The resonance can be damped passively by adding resistors connected in series or in parallel with the filter capacitor. However, this may introduce losses in the damping resistor and reduce the efficiency [4].

Various active damping control algorithms for grid-connected inverter with *LCL* filters have been investigated in recent years. In [5]–[10], the capacitor current feedback control is implemented, which provides the damping effect by creating a virtual resistor connected in parallel with the filter capacitor. The similar target can also be achieved by the capacitor voltage derivative feedback control [11]–[12]. In [13]–[16], the notch filter is also implemented to cancel the resonant peak from the control perspective. In [17], the converter-side and the grid-side current are simultaneously used as feedback states. By properly tuning the weighting factor, the third-order plant model can be reduced to a first-order model. In addition, active disturbance rejection controls (ADRCs) are also proposed to realize robust active damping [18]–[19].

For the electromechanical system like wind turbine generator (WTG), hybrid electrical propulsion for aerospace or marine system, there are power electronics converters connected to the generator and motor. The mechanical parts of such a system are not rigidly connected, for example, the motor rotor and load such as propeller are connected through coupling and gearbox used in the drivetrain. These mechanical connections formulate a multi-rotating mass system, where different masses are connected flexibly with a certain stiffnesses and damping coefficients. There are multiple resonance modes for the system, which can be excited in various transient conditions like sudden electromagnetic torque or load torque changes and cause drivetrain over torque with reduced lifetime.

Failure of the sensitive mechanical components such as couplings, bearings, and gear teeth are the most common faults associated with electromechanical systems. Active torsional vibration damping control was expected to protect the sensitive mechanical components against over torque using the speed or shaft torque feedback [20]–[31].

In 1990s, there were active damping control algorithms proposed for inverter-driven machine with multi-rotating mass [21]–[22]. However, researchers working on inverters with *LCL* filter active damping control in 2000s and early 2010s have overlooked the achievements made in mechanical torsional

This work was supported by Micro Electronics R&D center of Shenzhen Topband Co., Ltd under the Grant number 40121065. (*Corresponding author: Yang Qi*)

Xiong Liu and Yuanpeng Guan are with the Energy Electricity Research Center, International Energy College, Jinan University, Zhuhai, 510632, China. (email: liushawn123@ieee.org; guanyp@jnu.edu.cn)

Yang Qi is with the School of Automation, Northwestern Polytechnical University, China. (email: qiyang@nwpu.edu.cn)

Yi Tang and Peng Wang are with Nanyang Technological University, 639798, Singapore (email: yitang@ntu.edu.sg; epwang@ntu.edu.sg)

Frede Blaabjerg is with the Department of Energy Technology at Aalborg University, Denmark (email: fbl@et.aau.dk)

This article has been accepted for publication in a future issue of this journal, but has not been fully edited. Content may change prior to final publication. Citation information: DOI 10.1109/TIE.2021.3095796, IEEE Transactions on Industrial Electronics

vibration suppression control [1]–[2], [8]. On the other hand, researchers working on mechanical torsional vibration suppression control in recent years [25]–[28] have also ignored the latest research findings from active damping control for inverter with *LCL* filter.

In this paper, the mathematical models for the electrical *LCL* system and mechanical spring-mass system are analyzed together and compared systematically. Two typical active damping control algorithms for the *LCL* system (mechanical spring-mass system) including the capacitor current feedback (speed difference feedback) and the capacitor voltage derivative feedback (shaft torque derivative feedback) were investigated. The electrical and mechanical system models are found to be fundamentally the same, therefore, the active damping control structure, feedback parameters are the same except for different symbols used in different systems. In addition to the given examples, any other existing or future new active damping control algorithm in the electrical *LCL* system or mechanical spring-mass system can be applied to each other. This will help researchers working in either electrical or mechanical damping control area to have a wider scope of prior-arts in mind and avoid reinventing the wheel before trying to explore new control algorithms in the future.

For *LCL* system, the digital control delay effect caused by the sampling and modulation process will be considered and controller parameter sensitivity analysis will be performed. For the mechanical active damping control, the inverter needs to be designed carefully to handle the short-term overcurrent caused by the electromagnetic torque overshoot during the step load decrease event. The overshoot peak value was also calculated under various damping coefficients to guide inverter design in this paper.

II. Modeling of Inverter with *LCL* Filter and Motor Drive System with Multi-Rotating Mass Load

A. Inverter with LCL Filter

Fig. 1 shows a grid-connected three-phase inverter with an *LCL* filter. The state-space equations can be built based on Kirchhoff's voltage and current laws given as (1).

$$\frac{d}{dt}\begin{pmatrix} i_c \\ i_g \\ v_f \end{pmatrix} = \begin{pmatrix} 0 & 0 & -L_c^{-1} \\ 0 & 0 & L_g^{-1} \\ C_f^{-1} & -C_f^{-1} & 0 \end{pmatrix}\begin{pmatrix} i_c \\ i_g \\ v_f \end{pmatrix} + \begin{pmatrix} L_c^{-1} & 0 \\ 0 & -L_g^{-1} \\ 0 & 0 \end{pmatrix}\begin{pmatrix} v_c \\ v_g \end{pmatrix}, \quad (1)$$

where L_c is the converter-side filter inductance, L_g is the sum of grid-side filter inductance and feeder inductance; i_c and i_g are converter-side and grid-side current, respectively; v_c and v_g are converter voltage and grid voltage; C_f is the filter capacitance and v_f is the filter capacitor voltage.

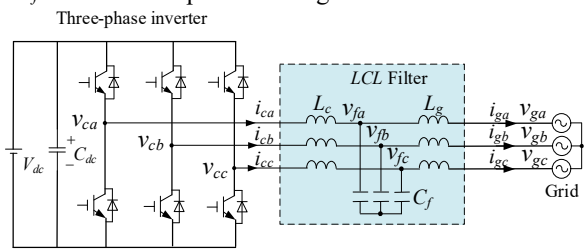

Fig. 1. Grid-connected three-phase inverter with *LCL* filter.

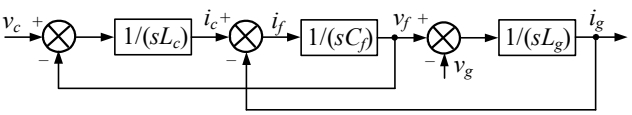

Fig. 2. Control plant block diagram of a three-phase inverter with *LCL* filter.

The *LCL* system control plant block diagram is established as shown in Fig. 2 based on the mathematical model of (1). The transfer function from the converter voltage v_c to filter capacitor voltage v_f can be derived as

$$\frac{v_f(s)}{v_c(s)} = \frac{1}{L_c C_f} \cdot \frac{1}{s^2 + (L_c + L_g)/(C_f L_c L_g)}. \quad (2)$$

The electrical system resonance frequency is calculated as

$$\omega_{re} = \sqrt{\frac{L_c + L_g}{C_f L_c L_g}}. \quad (3)$$

B. Inverter-driven Motor with Multi-rotating Masses

Fig. 3 shows the inverter-driven motor and mechanical load with two rotating masses. The mechanical transmission parts such as shaft, coupling, gear-box have elastic effects, which can be modelled as a lumped spring with a certain stiffness. The spring-mass system model is shown in Fig. 4.

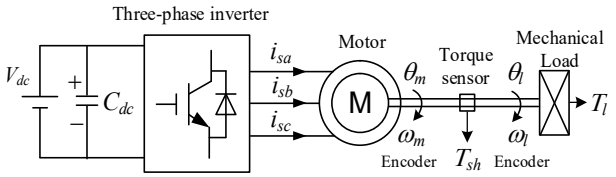

Fig. 3. Inverter-driven motor and mechanical load with two rotating masses.

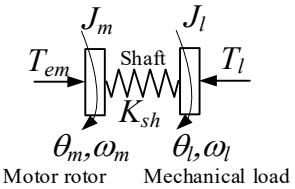

Fig. 4. Inverter-driven motor mechanical part spring-mass model.

The state-space equations can be built according to Newton's second law in the rotational form and Hooke's Law in the torsional form are given as (4).

$$\frac{d}{dt}\begin{pmatrix} \omega_m \\ \omega_l \\ T_{sh} \end{pmatrix} = \begin{pmatrix} 0 & 0 & -J_m^{-1} \\ 0 & 0 & J_l^{-1} \\ K_{sh} & -K_{sh} & 0 \end{pmatrix}\begin{pmatrix} \omega_m \\ \omega_l \\ T_{sh} \end{pmatrix} + \begin{pmatrix} J_m^{-1} & 0 \\ 0 & -J_l^{-1} \\ 0 & 0 \end{pmatrix}\begin{pmatrix} T_m \\ T_l \end{pmatrix}, \quad (4)$$

where J_m and J_l are machine rotor inertia and mechanical load inertia, respectively; ω_m and ω_l are machine and load rotating speed; T_{em} and T_l are the machine electromagnetic torque and mechanical load torque. K_{sh} is shaft stiffness and T_{sh} is the shaft torque.

The inertia J_m and J_l and stiffness K_{sh} (*JKJ*) system control plant block diagram can be established as shown in Fig. 5 based on the mathematical model in (4). The transfer function from electromagnetic torque T_{em} to shaft torque T_{sh} can be derived as

This article has been accepted for publication in a future issue of this journal, but has not been fully edited. Content may change prior to final publication. Citation information: DOI 10.1109/TIE.2021.3095796, IEEE Transactions on Industrial Electronics

TABLE I.
MAPPLING OF ELECTRICAL AND MECHANICAL SYSTEM PARAMETERS

Electrical Variables	Symbol	Mechanical Variables	Symbol
Converter voltage	v_c	Electromagnetic Torque	T_{em}
Converter side current	i_c	Machine speed	ω_m
Converter side inductance	L_c	Machine rotor inertia	J_m
Capacitor voltage	v_f	Shaft torque	T_{sh}
Capacitance	C_f	Reciprocal of stiffness	$1/K_{sh}$
Grid side current	i_g	Mechanical load speed	ω_l
Grid side inductance	L_g	Mechanical load inertia	J_l
Grid voltage	v_g	Mechanical load torque	T_l
Converter side inductor series resistance	R_c	Machine rotor friction coefficient	B_m
Grid side inductor series resistance	R_g	Mechanical load friction coefficient	B_l
Capacitor series resistance	R_f	Shaft material damping coefficient	D_{sh}

TABLE II.
COMPARISONS OF THE STATE-OF-THE-ART DAMPING METHODS FOR ELECTRICAL AND MECHANICAL SYSTEMS

Active damping methods	Mechanical System	Electrical System
Feedback-based appraoch	Speed difference feedback [29]	Capacitor current feedback [5]–[10]
	Motor speed feedback [25]	Converter-side current feedback [2]
	Torsional torque derivative feedback [21]	Capacitor voltage derivative feedback [11]–[12]
Nocth-filter-based approach	For the JKJ resonance [30]–[31]	For the LCL resonance [13]–[16]
Other approach	Active disturbance rejection control [32]	Active disturbance rejection control [19]

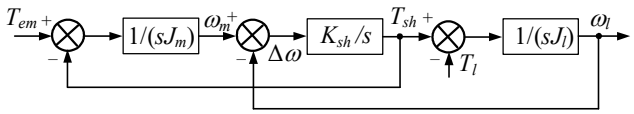

Fig. 5. Control plant block diagram for the two rotating mass system.

$$\frac{T_{sh}(s)}{T_{em}(s)} = \frac{K_{sh}}{J_m} \cdot \frac{1}{s^2 + K_{sh}(J_m + J_l)/(J_m J_l)}. \tag{5}$$

The mechanical system resonance frequency can be calculated as

$$\omega_{rm} = \sqrt{\frac{K_{sh}(J_m + J_l)}{J_m J_l}}. \tag{6}$$

From the above analysis, it is found that the mathematical models between electrical and mechanical systems are almost the same, where the only differences are the symbols used in different systems. Table I summarizes a one-to-one mapping of the electrical and mechanical system parameters, which also includes the parameters like the electrical resistances and mechanical friction coefficients etc. On this basic, the state-of-the-art research findings in both electrical systems and mechanical systems are summarized and listed in Table II.

III. UNIFIED ACTIVE DAMPING ALGORITHM

A. Active damping for LCL Electrical System

Equation (2) can be rewritten as,

$$v_f(s) = v_c(s) \cdot \frac{1}{L_c C_f} \cdot \frac{1}{s^2 + \omega_{re}^2}. \tag{7}$$

One straightforward method for the resonance damping is to use the converter-side current feedback control. Fig. 6 illustrates the control block diagram, where k_{pi} and k_{ii} are the proportional and integral control gains.

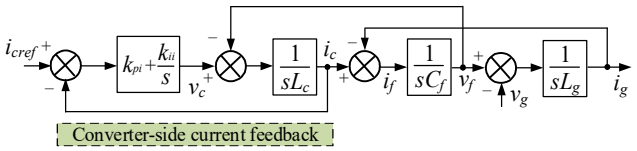

Fig. 6. Active damping control using converter-side current feedback of system shown in Fig. 1.

It should be highlighted that the PWM inverter has a transfer function of $K_{\mathrm{PWM}}=V_{\mathrm{dc}}/V_{\mathrm{tri}}$, whereas V_{dc} is the inverter DC-link voltage, and V_{tri} is the peak-to-peak amplitude of the triangular carrier. In the following analysis for both electrical and mechanical systems, the system control outputs are divided by K_{PWM} before sending as the PWM modulation references. By doing so, the control parameter design will not be interfered by the effect of K_{PWM} and the mathematical equations will also be simplified without containing the parameter K_{PWM}.

The *LCL* plant model is derived as

$$G_{ic}(s) = \frac{i_c(s)}{v_c(s)} = \frac{C_f L_g s^2 + 1}{L_g L_c C_f s} \cdot \frac{1}{s^2 + \omega_{re}^2}. \tag{8}$$

According to (8), the system open-loop transfer function can be expressed as

$$G_{oe1}(s) = \frac{i_c(s)}{v_c(s)}\left(k_{pi} + \frac{k_{ii}}{s}\right) = \frac{k_{pi} C_f L_g s^3 + k_{ii} C_f L_g s^2 + k_{pi} s + k_{ii}}{L_g L_c C_f s^4 + (L_g + L_c) s^2}. \tag{9}$$

This article has been accepted for publication in a future issue of this journal, but has not been fully edited. Content may change prior to final publication. Citation information: DOI 10.1109/TIE.2021.3095796, IEEE Transactions on Industrial Electronics

Fig. 7 shows the root locus of converter current feedback control with a particular ratio of k_{pi} and k_{ii}. It is observed that the conjugated poles associated with LCL resonance are located in the left-half plane. This indicates that an inherent damping effect is created through the feedback of converter-side current i_c. However, the damping coefficient of the conjugated poles cannot be arbitrarily adjusted and it will be restricted by a limit ζ_{max}. Even though the system stability is ensured, the dynamic performance may still be oscillatory if ζ_{max} is much smaller than 1. Notice that the locations of open-loop zeros will change according to the ratio of k_{pi} and k_{ii}. However, it has been tried that no matter how we place the open-loop zeros introduced by the PI controller, the closed-loop system has a limited damping coefficient through the root-locus analysis.

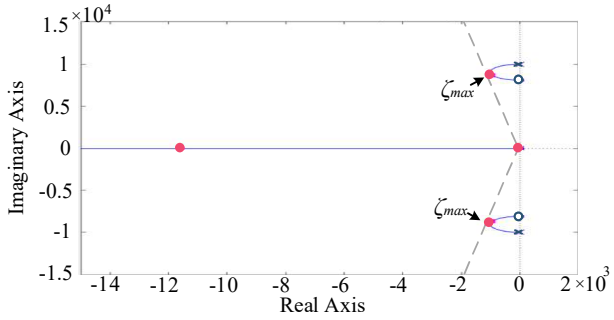

Fig. 7. Root locus plot of the converter-side current feedback control with L_g = 1 mH, L_c = 2 mH, C_f = 15 μF.

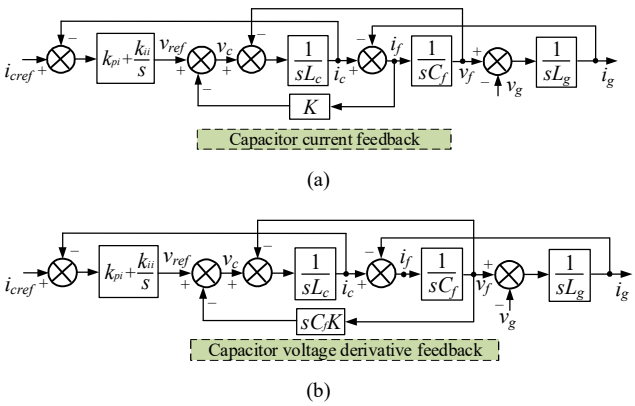

Fig. 8. Active damping schemes for electrical systems. (a). Capacitor current feedback. (b). Capacitor voltage derivative feedback.

To address this issue, the capacitor current or the derivative of capacitor voltage can be further used to improve the damping performance. Fig. 8(a) shows the control block diagram using the capacitor current feedback with a feedback gain K. If the capacitor voltage derivative feedback is used, the differentiator gain is equivalent to $C_f K$, as shown in Fig. 8(b). The current loop plant is given as equation (10)

$$\frac{i_c(s)}{v_{ref}(s)} = \frac{C_f L_g s^2 + 1}{L_g L_c C_f s} \cdot \frac{1}{s^2 + \frac{K}{L_c} s + \omega_{re}^2}. \tag{10}$$

Compared with (8), the denominator in (10) includes an extra 's' term, which dampens the LCL resonance. The modified system open-loop transfer function is derived as

$$G_{oe2}(s) = \frac{k_{pi} C_f L_g s^3 + k_{ii} C_f L_g s^2 + k_{pi} s + k_{ii}}{L_g L_c C_f s^4 + K L_g C_f s^3 + (L_g + L_c) s^2}. \tag{11}$$

Fig. 9 shows the root locus plot of capacitor-current feedback control. It can be observed that the maximum damping ratio of the conjugated poles can be greater than unity through a proper design of control parameters. In other words, a critical damping ratio (ζ =1) can be realized and undesired oscillations can be avoided in the system.

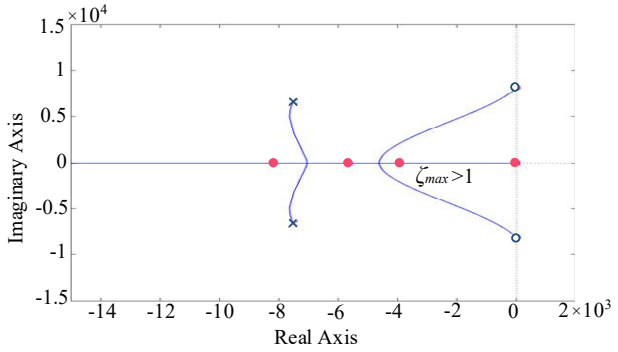

Fig. 9. Root locus of capacitor current feedback control when K=1.5$L_c\omega_{re}$.

By setting the same ratio of k_{ii}/k_{pi} =10, the root loci are plotted in Fig. 10 for different capacitor current feedback gain K. It can be seen that with the increasement of K, the open-loop complex-conjugate poles are moving away from the imaginary axis, which will lead to different root loci of the system for closed-loop poles.

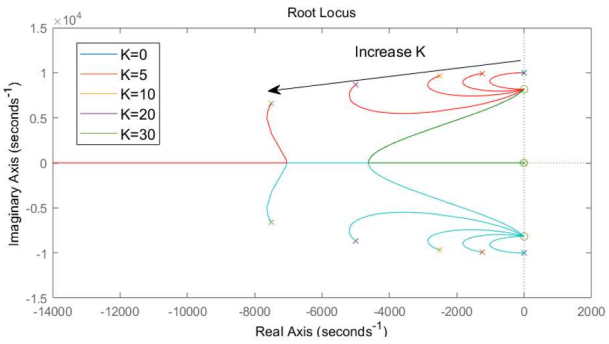

Fig. 10. Root loci plots for electrical system with different capacitor current feedback gain K by keeping k_{ii}/k_{pi} =10.

B. Active damping for JKJ Mechanical System

To move into the mechanical domain, equation (5) can be rewritten as

$$T_{sh}(s) = T_{em}(s) \cdot \frac{K_{sh}}{J_m} \cdot \frac{1}{s^2 + \omega_{rm}^2}. \tag{12}$$

Fig. 11 illustrates the control block diagram of an induction machine under the speed control mode. ω_{m_ref} is the reference machine speed, $k_{p\omega}$ is the proportional control gain and $k_{i\omega}$ is the integral control gain. To avoid unnecessary complications, the dynamics of the motor drive inner-loop current controls are neglected such that T_{em} is equal to its reference and the inner torque (current) closed-loop transfer function can be treated as unity. This simplification is reasonable since the inner-loop control bandwidth is much larger than the outer loop (speed

This article has been accepted for publication in a future issue of this journal, but has not been fully edited. Content may change prior to final publication. Citation information: DOI 10.1109/TIE.2021.3095796, IEEE Transactions on Industrial Electronics

regulation). Based on Fig. 11, the transfer function from the electromagnetic torque to machine speed is derived as

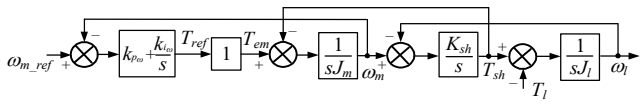

Fig. 11. Control block diagram of the induction machine with two masses.

$$\frac{\omega_m(s)}{T_{em}(s)}=\frac{K_{sh}^{-1}J_l s^2+1}{J_l J_m K_{sh}^{-1} s}\cdot\frac{1}{s^2+\omega_{rm}^2}. \tag{13}$$

The system open-loop transfer function is given by

$$G_{om1}(s)=\frac{k_{p\omega}K_{sh}^{-1}J_l s^3+k_{i\omega}K_{sh}^{-1}J_l s^2+k_{p\omega}s+k_{i\omega}}{J_m J_l K_{sh}^{-1}s^4+(J_m+J_l)s^2}. \tag{14}$$

Fig. 12 shows the root locus plot of $G_{om1}(s)$ with a particular ratio of $k_{p\omega}$ and $k_{i\omega}$. Although the system is stable, the damping ratio of the conjugated poles is always less than unity no matter how the speed PI controller open-loop pole is placed. The result of mechanical system root-locus plot is similar to the electrical system shown in Fig. 7.

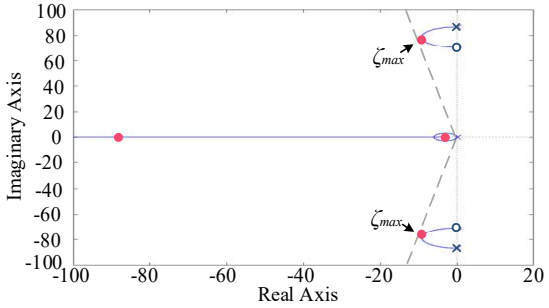

Fig. 12. Root locus plot of mechanical system with J_m=0.2 kg·m^2, J_l = 0.1 kg·m^2, and K_{sh}=500 N·m/rad.

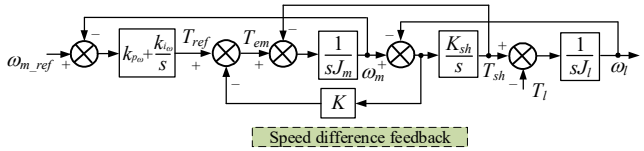

(a)

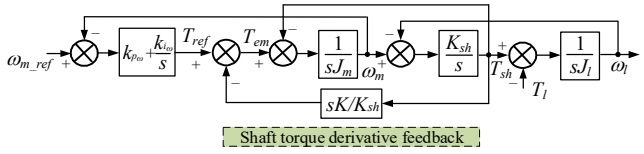

(b)

Fig. 13. Active damping schemes for mechanical systems. (a). Speed difference feedback. (b). Shaft torque derivative feedback.

To increase the damping ratio, the speed difference feedback or the shaft torque derivative feedback can be applied, as shown in Fig. 13(a) and Fig. 13(b), respectively. The transfer function from the machine reference torque to shaft torque can be derived as

$$T_{em}(s)=T_{ref}(s)-s\cdot\frac{K}{K_{sh}}T_{sh}(s), \tag{15}$$

$$\frac{T_{sh}(s)}{T_{ref}(s)}=\frac{K_{sh}}{J_m}\cdot\frac{1}{s^2+s\cdot\frac{K}{J_m}+\omega_{rm}^2}. \tag{16}$$

Compared with (12), the denominator in (16) includes an extra 's' term, which dampens the mechanical resonance by the feedback gain K. The transfer function from machine reference torque to rotor speed is derived as

$$\frac{\omega_m(s)}{T_{ref}(s)}=\frac{J_l K_{sh}^{-1}\cdot s^2+1}{J_l J_m K_{sh}^{-1}\cdot s}\cdot\frac{1}{s^2+\frac{K}{J_m}s+\omega_{rm}^2}. \tag{17}$$

Based on this, the mechanical system open-loop transfer function is given by

$$G_{om2}(s)=\frac{k_{p\omega}K_{sh}^{-1}J_l\cdot s^3+k_{i\omega}K_{sh}^{-1}J_l\cdot s^2+k_{p\omega}\cdot s+k_{i\omega}}{J_l J_m K_{sh}^{-1}\cdot s^4+KJ_l K_{sh}^{-1}\cdot s^3+(J_l+J_m)\cdot s^2}. \tag{18}$$

Fig. 14 shows the root locus with active damping controls. It is observed that the maximum damping ratio of the conjugated poles can be adjusted greater than unity, just like the scenario of the electrical *LCL* system with active damping control.

It should be mentioned that in some applications the machine is operated in the torque control mode without an outer speed loop. In that case, the electromagnetic torque reference is provided to the motor control system, and the same active damping control using the speed difference or the shaft torque derivative feedback can still be used.

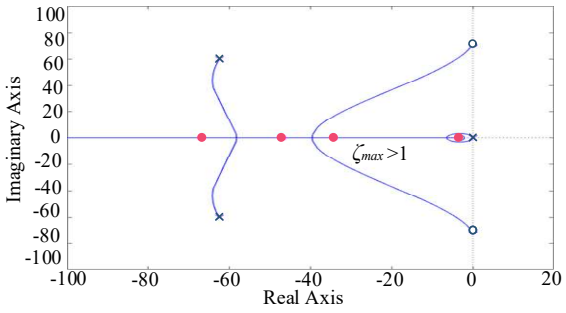

Fig. 14. Root locus of speed difference feedback control when K=1.5$J_m\omega_{rm}$.

C. Unified Active Damping Control for Electrical and Mechanical System

Comparing (10) and (17), it can be found that the third order control plants for electrical and mechanical systems were modified, where the complex-conjugate open-loop poles were moved away from the imaginary axis with a damping term. From the control perspective, as long as control plant state-space equations are the same, the active damping control structures, feedback parameters, open and closed-loop transfer functions are also the same. Therefore, the active damping algorithms used in an electrical *LCL*-based system can be applied to the mechanical system and vice versa.

Note that this paper uses two examples to demonstrate the high similarity between the two systems. Other existing control methods such as active damping control using a notch filter are not covered in the analysis of this paper but could have the same high degree of similarity between the two systems.

This article has been accepted for publication in a future issue of this journal, but has not been fully edited. Content may change prior to final publication. Citation information: DOI 10.1109/TIE.2021.3095796, IEEE Transactions on Industrial Electronics

IV. Different Characteristics for Electrical and Mechanical Active Damping Control

It should be noted that the resonance frequency of electrical *LCL* system is much higher than the mechanical *JKJ* system. The digital control delay effect caused by the sampling and modulation process for *LCL* system has considerable impact on system stability [5]–[7] which will be analyzed below. The delay impact for mechanical *JKJ* system is ignorable since the mechanical resonance frequency is relatively low. However, to damp the mechanical resonance, the electromagnetic torque will have overshoots and maybe oscillations, which will be calculated quantitatively in the following section.

A. Digital Control System Analysis for Electrical Active Damping

The active damping scheme using capacitor current feedback with the control plant in the continuous *s* domain and discrete *z* domain is illustrated in Fig. 15. The transfer function $G_h(s)$ for zero-order hold (ZOH) is expressed as

$$G_h(s)=\frac{1-e^{-Ts}}{s}. \tag{19}$$

In order to analyze the control system in discrete *z*-domain, the *Z* transformation for control plants $G_{ic}(s)$ and $G_{if}(s)$ with ZOH should be applied. The transfer function for $G_{ic}(s)$ and $G_{if}(s)$ in the continuous *s* domain are expressed as

$$\begin{cases} G_{ic}(s)=\dfrac{i_c(s)}{v_c(s)}=\dfrac{C_f L_g s^2+1}{L_g L_c C_f s}\cdot\dfrac{1}{s^2+\omega_{re}^2} \\ G_{if}(s)=\dfrac{i_f(s)}{v_c(s)}=\dfrac{s}{L_c}\cdot\dfrac{1}{s^2+\omega_{re}^2} \end{cases}. \tag{20}$$

Through the ZOH *Z* transformation, the transfer functions for control plant $G_{ic}(z)$ and $G_{if}(z)$ can be derived as below,

$$\begin{aligned} G_{ic}(z)&=Z[G_h(s)\cdot G_{ic}(s)] \\ &=\frac{1}{(L_c+L_g)}\cdot\frac{T}{(z-1)}+\frac{L_g\cdot\sin(\omega_{re}T)}{L_c(L_c+L_g)\omega_{re}}\cdot\frac{(z-1)}{z^2-2z\cdot\cos(\omega_{re}T)+1}. \end{aligned} \tag{21}$$

$$G_{if}(z)=Z[G_{ZOH}(s)\cdot G_{if}(s)]=\frac{\sin(\omega_{re}T)}{L_c\omega_{re}}\cdot\frac{z-1}{z^2-2z\cdot\cos(\omega_{re}T)+1}. \tag{22}$$

The overall control block diagram for electrical system in the discrete *z* domain is shown in Fig. 16.

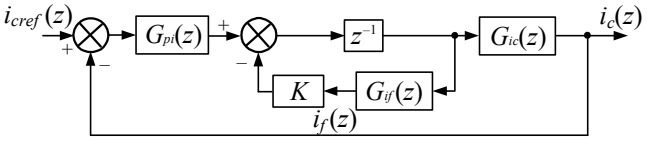

Fig. 16. Active damping schemes for electrical system in discrete *z* domain.

The control plant transfer function for the discretized system can be derived as shown in (23). The electrical system open loop transfer function $G_{oe}(z)$ is the multiplication of transfer functions of PI controller $G_{pi}(z)$ and system plant $G_p(z)$. The PI controller doesn't have any pole located outside the unit circle. Therefore, the number of poles located outside the unit circle for $G_{oe}(z)$ is determined by the characteristic equation below,

$$(z^2-2z\cdot\cos(\omega_{re}T)+1)\cdot z+\frac{K\cdot\sin(\omega_{re}T)}{\omega_{re}L_c}\cdot(z-1)=0. \tag{24}$$

Use the transformation $z=(1+w)/(1-w)$ to map the unit circle of *z*-domain to the imaginary axis of *w*-domain, then apply Routh stability criterion. By doing this, it can be derived that if the capacitor current feedback current feedback gain *K* meets the requirement in (25), there are two sign changes for the first column of Routh array indicating two poles on the right plane. Otherwise, there is no pole located on the right plane. $K_{\lim}$ is calculated to be 31.503 based on the parameters in Table III.

$$K>K_{\lim}=\frac{2\cos(\omega_{re}T)-1}{\sin(\omega_{re}T)}\omega_{re}L_c \tag{25}$$

TABLE III
Electrical System Parameter Values

Parameters	Descriptions	Values
V_{dc}	DC-link voltage	200 V
V_g	Grid voltage magnitude	75 V
f_g	Grid frequency	50 Hz
L_c	Converter-side inductance	2 mH
L_g	Grid-side inductance	1 mH
C_f	Filter capacitance	15 μF
k_{pi}	Proportional gain	2.5
k_{ii}	Integral gain	25
f_{sw}	Switching frequency	20 kHz
K	Capacitor current feedback gain	10

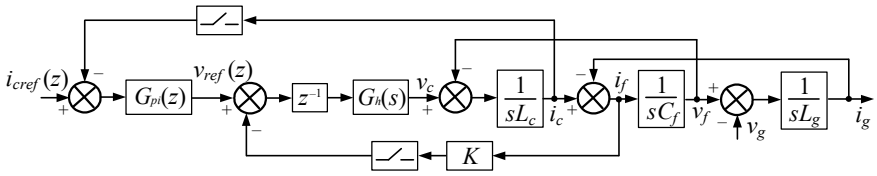

Fig. 15. Active damping schemes for electrical system using capacitor current feedback in the mixed s- and z- domain.

$$G_p(z)=\frac{z^{-1}}{1+z^{-1}\cdot K\cdot G_{if}(z)}\cdot G_{ic}(z)=\frac{L_c\omega_{re}T(z^2-2z\cdot\cos(\omega_{re}T)+1)+L_g\cdot\sin(\omega_{re}T)(z-1)^2}{\omega_{re}L_c(L_c+L_g)(z-1)[(z^2-2z\cdot\cos(\omega_{re}T)+1)\cdot z+\frac{K\cdot\sin(\omega_{re}T)}{\omega_{re}L_c}\cdot(z-1)]}. \tag{23}$$

This article has been accepted for publication in a future issue of this journal, but has not been fully edited. Content may change prior to final publication. Citation information: DOI 10.1109/TIE.2021.3095796, IEEE Transactions on Industrial Electronics

If $K<K_{\text{lim}}$, choose K=10 as an example, the Nyquist diagrams are plotted in Fig. 17 when the PI controller gains were changed while the ratio of k_{ii}/k_{pi} =10 was kept constant. The number of the right plane poles of the open-loop transfer function is 0. For k_{pi}=2.5, 10, 20, the number of counter clockwise encirclements of (–1, j0) point is also 0, so the system is stable according to Nyquist Stability Criterion. The system will become unstable when k_{pi} was further increased. For k_{pi}=40, the number of clockwise encirclements of (–1, j0) point is 2, which means the system is unstable and there are two right plane closed-loop poles.

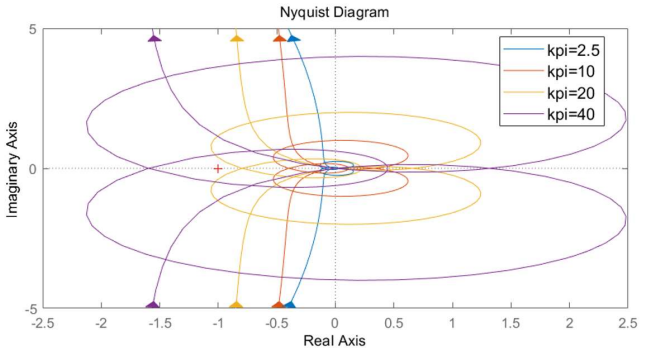

Fig. 17. System open-loop Nyquist diagrams when K=10 for different PI controller gain with constant ratio of k_{ii}/k_{pi}=10.

If $K>K_{\text{lim}}$, choose K=35 as an example, the Nyquist diagrams are plotted in Fig. 18 when the PI controller gains were changed while the ratio of k_{ii}/k_{pi} =10 was kept constant. The number of the right plane poles of the open-loop transfer function is 2. For any k_{pi} value, the number of counterclockwise encirclements of (–1, j0) point is 0, which doesn't satisfy the Nyquist Stability Criterion and the system is unstable.

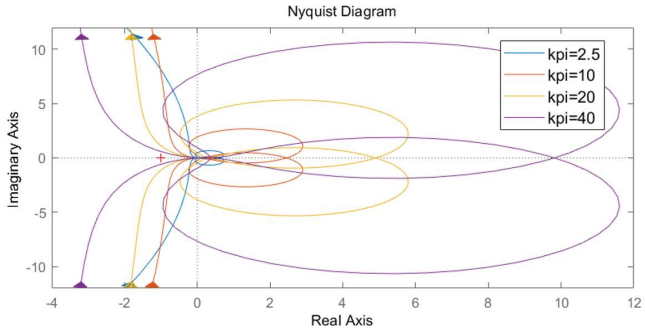

Fig. 18. System open-loop Nyquist diagrams when K=35 for different PI controller gain with constant ratio of k_{ii}/k_{pi}=10.

Without capacitor current feedback, the parameter sensitivity analysis for different PI controller gains was performed by plotting various step responses for the closed-loop electrical system as shown in Fig. 19 and Fig. 20. There is a tradeoff between the system overshoot and the control bandwidth. The parameters k_{pi} =2.5, k_{ii} =25 are selected in this paper which will cause a small overshoot as seen from the plot.

By fixing the ratio of k_{ii}/k_{pi} =10, the root loci in discrete domain are plotted in Fig. 21. It can be seen that when K=30, the complex-conjugate poles are very close to the unit circle and it will easily become unstable with very small gain k_{pi}=1.73.

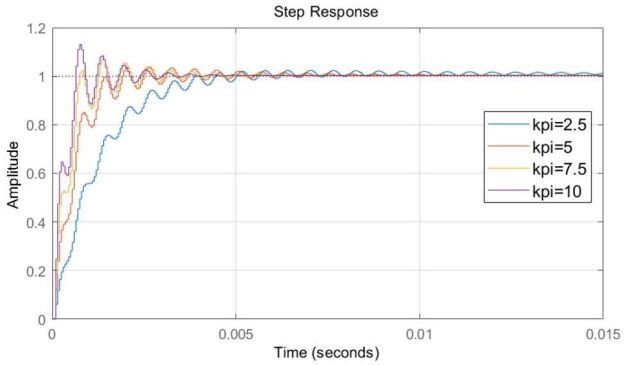

Fig. 19. Step responses for the closed-loop electrical system with increasement of k_{pi} (k_{ii}/k_{pi} =10, K=0).

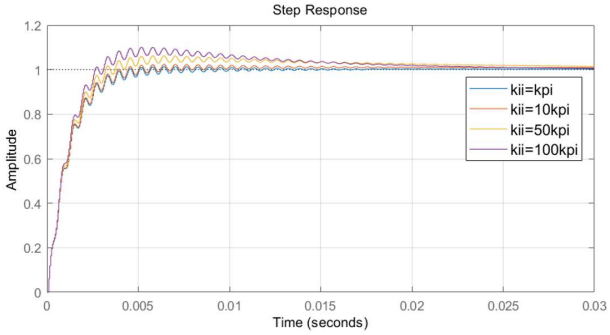

Fig. 20. Step responses for the closed-loop electrical system with different ratios of k_{ii}/k_{pi} (k_{pi}=2.5, K=0).

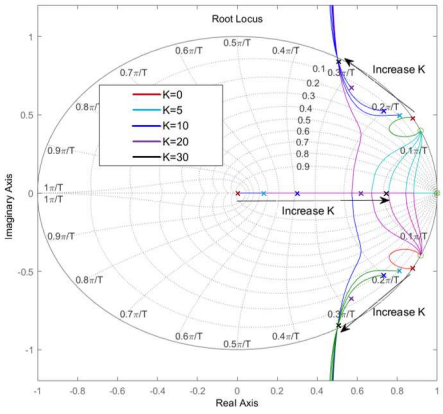

Fig. 21. Root loci plots for electrical system in discrete domain with different capacitor current feedback gain K (k_{ii}/k_{pi} =10).

By setting the parameters k_{pi} =2.5, k_{ii} =25, the closed-loop electrical system pole-zero maps and step responses are plotted for different K values as shown in Fig. 22 and Fig. 23 respectively. It can be seen that when K was increased from 0 to 10, the damping ratio for complex-conjugate closed-loop poles was increased from 0.017 to 0.201. The knee point is around K=10 since when K was increased from 10 to 25, the damping ratio was decreased from 0.201 to 0.0506. When K=30, the system became unstable as two closed-loop system poles are moving outside the unit circle.

This article has been accepted for publication in a future issue of this journal, but has not been fully edited. Content may change prior to final publication. Citation information: DOI 10.1109/TIE.2021.3095796, IEEE Transactions on Industrial Electronics

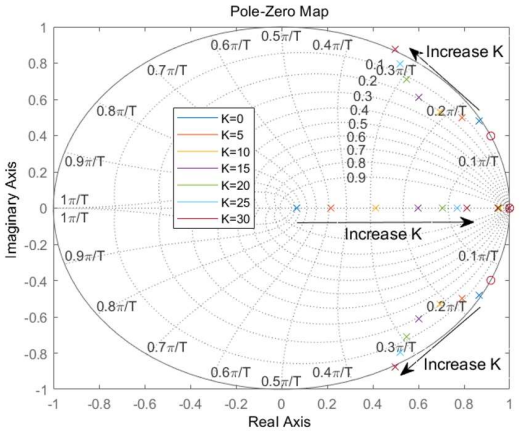

Fig. 22. Closed-loop electrical system pole-zero maps with increasement of K (k_{pi} =2.5, k_{ii} =25).

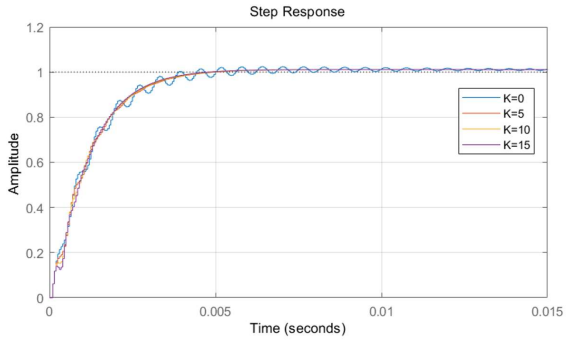

Fig. 23. Step response for closed-loop electrical system with different capacitor current feedback gain K (k_{pi} =2.5, k_{ii}=25).

It should be noted that the similar parameter sensitivity analysis can also be performed for the mechanical system, which will not be elaborated due to the page limit.

B. Calculation of Electromagnetic Torque Overshoot When Applying Mechanical Active Damping

The essence behind the mechanical damping is to change the electromagnetic torque fast enough to suppress the shaft torque oscillation. It is to sacrifice electromagnetic torque overshoot/ stator over current to save the mechanical drivetrain lifetime. It is reasonable to do so as mechanical component maintenance is normally much more difficult than electrical one, for example the marine thruster drivetrain underwater or dry dock maintenance. The short time overcurrent is acceptable for electrical machines, but the inverter needs to be designed carefully to handle this.

It can be seen from Fig. 5 that the shaft torque T_{sh} is determined by the electromagnetic torque T_{em} and load torque T_l, the transfer function relationship among them can be derived below using the superposition principle.

$$T_{sh}(s)=\frac{K_{sh}}{J_m}\cdot\frac{1}{s^2+\omega_{rm}^2}T_{em}(s)+\frac{K_{sh}}{J_l}\cdot\frac{1}{s^2+\omega_{rm}^2}T_l(s). \quad (26)$$

After implementing the active damping control algorithm as shown in Fig. 13, the electromagnetic torque can be expressed below by substituting (26) into (15).

$$T_{em}(s)=\frac{s^2+\omega_{rm}^2}{s^2+s\cdot\frac{K}{J_m}+\omega_{rm}^2}\cdot T_{ref}(s)-\frac{sK}{J_l}\cdot\frac{1}{s^2+s\cdot\frac{K}{J_m}+\omega_{rm}^2}\cdot T_l(s) \quad (27)$$

Define damping coefficient ζ and damped natural frequency ω_d as below

$$2\zeta\omega_{rm}=\frac{K}{J_m},\qquad \omega_d^2=(1-\zeta^2)\omega_{rm}^2. \quad (28)$$

Equation (27) can be rewritten as

$$T_{em}(s)=\underbrace{\frac{s^2+\omega_{rm}^2}{s^2+2\zeta\omega_{rm}s+\omega_{rm}^2}\cdot T_{ref}(s)}_{First\ \ part}-\underbrace{\frac{J_m}{J_l}\cdot\frac{2\zeta\omega_{rm}s}{\omega_d}\cdot\frac{\omega_d}{(s+\zeta\omega_{rm})^2+\omega_d^2}\cdot T_l(s).}_{Second\ \ part} \quad (29)$$

The transient response of T_{em} is not only determined by the response of T_{ref}, but also superimposed by the second part of (29). The transfer function from load torque to reference torque can be derived as shown in (30) based on the control block diagram in Fig. 13. When the active damping control is enabled, additional electromagnetic torque T_{em_ad} overshoot/undershoot and oscillations are introduced, which can be calculated and analyzed below.

$$T_{em\_ad}(s)=\frac{J_m}{J_l}\cdot\frac{2\zeta\omega_{rm}s}{\omega_d}\cdot\frac{\omega_d}{(s+\zeta\omega_{rm})^2+\omega_d^2}\cdot T_l(s). \quad (31)$$

$$T_l(s)=\frac{\Delta T_l}{s}. \quad (32)$$

Based on the Laplace inverse transformation, the time-domain expression of additional electromagnetic torque can be derived in (33)

$$T_{em\_ad}(t)=2\Delta T_l\cdot\frac{J_m}{J_l}\cdot\frac{\zeta\omega_{rm}}{\omega_d}\cdot e^{-\zeta\omega_{rm}t}\cdot\sin(\omega_d t). \quad (33)$$

If the damping coefficient ζ is designed to be unity to achieve critical damping, the time-domain additional electromagnetic torque equation is expressed in (34).

$$T_{em\_ad}(t)=2\Delta T_l\cdot\frac{J_m}{J_l}\cdot\omega_{rm}\cdot e^{-\omega_{rm}t}\cdot t. \quad (34)$$

Considering the extreme case, when the machine is 100% loaded in steady state, the electromagnetic torque, shaft torque and load torque are the same and equal to the machine rated torque T_{rate}. Suddenly, the load torque is reduced to be 0 (for example, the marine propeller blades lift out of water in a high sea heavy weather condition during vessel operation) and ΔT_l equals to $-T_{rate}$, active damping control is enabled, otherwise the system will suffer from severe shaft torque torsional vibrations. By setting derivative of T_{em_ad} in (33) and (34) with respect to 't' to be zero, the peak value of T_{em_ad} and

$$T_{ref}(s)=\frac{Kk_{p\omega}s^2+(Kk_{i\omega}+k_{p\omega}K_{sh})s+K_{sh}k_{i\omega}}{J_mJ_ls^4+J_l(K+k_{p\omega})s^3+(J_mJ_l\omega_{rm}^2+k_{i\omega}J_l)s^2+k_{p\omega}K_{sh}s+K_{sh}k_{i\omega}}\cdot T_l(s). \quad (30)$$

This article has been accepted for publication in a future issue of this journal, but has not been fully edited. Content may change prior to final publication. Citation information: DOI 10.1109/TIE.2021.3095796, IEEE Transactions on Industrial Electronics

corresponding time 't_p' can be figured out.

$$T_{pem\_ad} = 2\Delta T_l \cdot \frac{J_m}{J_l} \cdot \zeta \cdot e^{-\zeta \cdot \frac{\sin^{-1}(\sqrt{1-\zeta^2})}{\sqrt{1-\zeta^2}}} \quad (0 \le \zeta < 1). \quad (35)$$

$$t_p = \frac{1}{\omega_{rm}} \cdot \frac{\sin^{-1}(\sqrt{1-\zeta^2})}{\sqrt{1-\zeta^2}} \quad (0 \le \zeta < 1). \quad (36)$$

The time-domain response of the additional electromagnetic torque is plotted in Fig. 24 at different damping coefficients. It is found that the larger the damping coefficient ζ, the higher the peak value of T_{em_ad}. When the damping coefficient ζ=1, peak value of T_{em_ad} reaches its maximum limit at t=1/ω_{rm} as described below.

$$T_{pem\_ad\max} = \frac{2}{e} \cdot \Delta T_l \cdot \frac{J_m}{J_l} \quad (\zeta = 1). \quad (37)$$

The peak torque value contributed by the second part of (29) was reached in a very short time duration while the first part torque was decreasing relatively slowly in speed control mode as shown in Fig. 25 during a unity load step decrease event. The torque responses in Fig. 25 are based on the parameters in Table IV. The full electromagnetic torque response is the summation of the first and the second part responses, whose peak value is close to but smaller than the original torque plus the peak of T_{em_ad}. If the machine is operating in torque control mode, the electromagnetic torque peak value equals the original torque plus the peak value of T_{em_ad} considering constant torque reference.

It can be seen from (37) that the maximum value of T_{em_ad} is determined by the machine rotor to mechanical load inertia ratio J_m/J_l. Substituting $\Delta T_l = -T_{rate}$ into (37) and add the original electromagnetic torque T_{rate}, the total electromagnetic torque can reach $(1+(2/e)\times J_m/J_l)$ times rated torque T_{rate} when unity active damping control is implemented. If the inertia ratio J_m/J_l is 1, the electromagnetic torque will reach 173.6% of rated torque; if the inertia ratio is larger than 1, for example J_m/J_l =2, the electromagnetic torque could reach 247.2% of rated torque. Therefore, there is a tradeoff between torsional vibration active damping control performance and inverter current rating. It should be noted that the overcurrent time duration is determined by the mechanical resonance frequency ω_{rm} and the damping coefficient ζ, so the inverter shall be designed properly to ensure its device junction temperature should not exceed its operation range during this transient process. Quantitative analysis in this section can be utilized as a guidance to evaluate conduction/ switching losses and junction temperature rise for inverter power semiconductor selection and cooling system design. The inverter can perform full active damping control with a large damping coefficient under light or medium load condition while the damping coefficient can be decreased under heavy load condition to keep the inverter current within a safety range.

TABLE IV

MECHANICAL SYSTEM PARAMETER VALUES

Parameters	Descriptions	Values
V_{dc}	DC-link voltage	700 V
P_N	Power rating	15 kW
R_s	Stator resistance	0.22 Ω
R_r	Rotor resistance	0.28 Ω
L_{ls}	Stator leakage inductance	2.8 mH
L_{lr}	Rotor leakage inductance	3.7 mH
L_m	Magnetizing inductance	82 mH
f_g	Grid frequency	50 Hz
P	Pole pairs	2
J_m	Rotor inertia	0.2 kg·m^2
J_l	Load inertia	0.1 kg·m^2
K_{sh}	Shaft stiffness	500 N·m/rad
λ_{r_ref}	Rotor flux reference	0.95 Wb
$k_{p\omega}$	Proportional gain (speed ctrl.)	5
$k_{i\omega}$	Integral gain (speed ctrl.)	30
f_{sw}	Switching frequency	20 kHz
K	Speed difference feedback gain	15

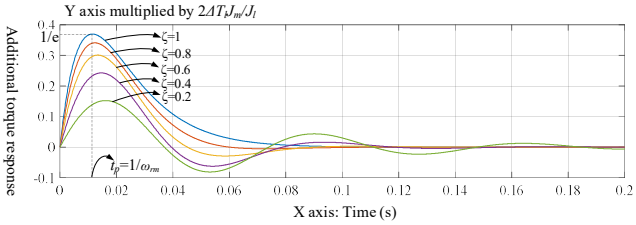

Fig. 24. Additional electromagnetic torque response at damping coefficients ζ.

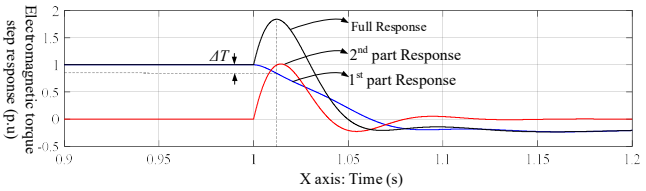

Fig. 25. Electromagnetic torque transient response during a unity load step decrease in speed control mode.

V. EXPERIMENTAL RESULTS

A. LCL Electrical System

To verify the theoretical findings and the effectiveness of *LCL* active damping, experiments were conducted using the hardware prototype shown in Fig. 26. The electrical system parameter values are listed in Table III.

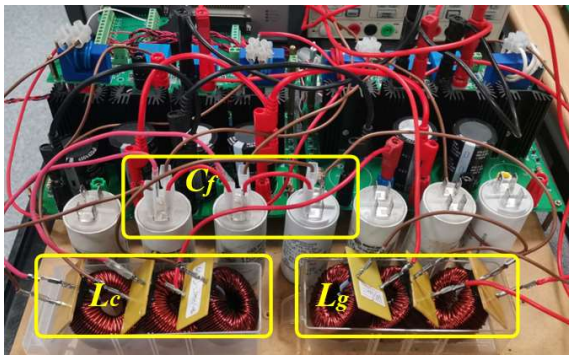

Fig. 26. Photo of the hardware setup of the *LCL*-filtered voltage source inverter.

Fig. 27 and Fig. 28 respectively illustrate the grid-side and converter-side current waveforms when K=0. It should be noted that the q-axis reference current is set as 0 A. It can also be set to $\omega_0 C_f v_g$ in order to achieve unity power factor operation [2]. The d-axis reference current is commanded to have a 2–4 A step

This article has been accepted for publication in a future issue of this journal, but has not been fully edited. Content may change prior to final publication. Citation information: DOI 10.1109/TIE.2021.3095796, IEEE Transactions on Industrial Electronics

increase. Due to inadequate damping of the *LCL* resonance, some high-frequency current oscillations are identified in Fig. 27 and Fig. 28.

As a contrast, Fig. 29 and Fig. 30 show the grid-side current and converter-side current waveforms when capacitor currents are utilized as additional feedbacks (K=10). The dynamic performance and stability is improved with the high-frequency current oscillations being effectively damped.

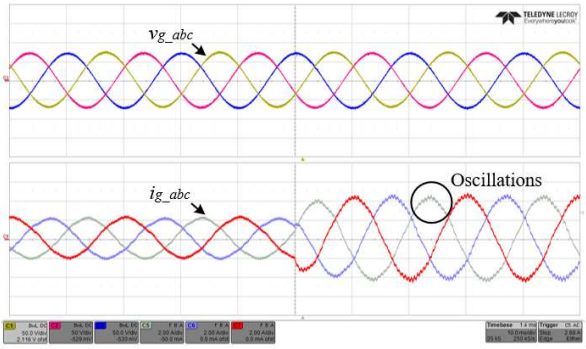

Fig. 27. Measured grid-side current waveforms after a disturbance (K=0).

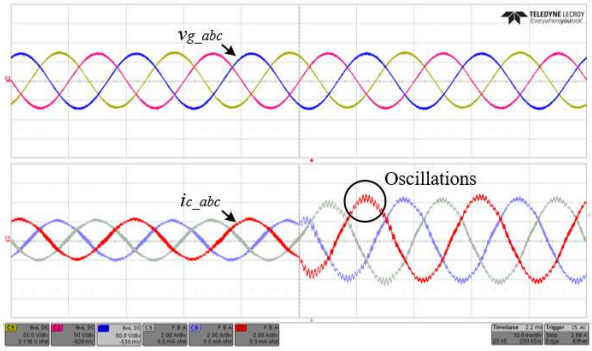

Fig. 28. Measured converter-side current waveforms after a disturbance (K=0).

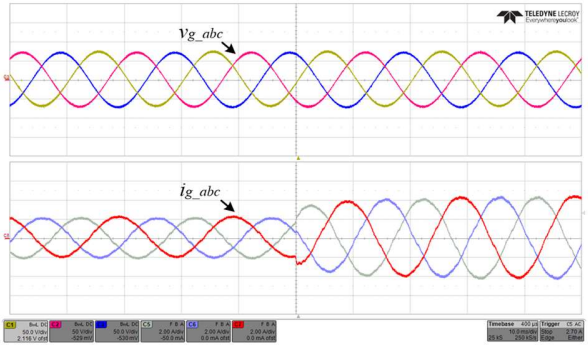

Fig. 29. Measured grid-side current waveforms after a disturbance (K=10).

B. JKJ Mechanical System

Next, a two-mass inverter-driven motor was constructed and tested through hardware-in-loop (HIL) platform. Fig. 31 shows the photo of the testing platform. On one hand, the mechanical plant was established within a PLECS RT-box with a discrete-time step of 2 μs. The plant model contains an induction motor, a shaft, a load mass, two speed sensors, and a load torque. On the other hand, the controller was implemented through a digital processor (TI Launchpad) with a sampling time of 50 μs.

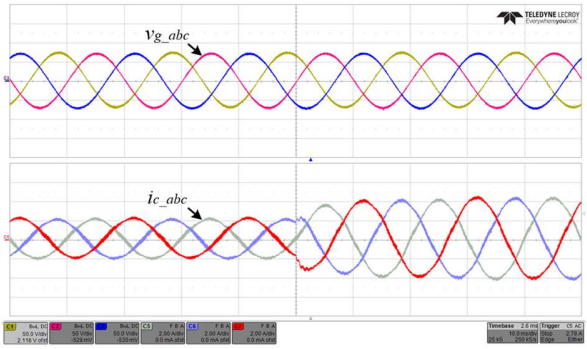

Fig. 30. Measured converter-side current waveforms after a disturbance (K=10).

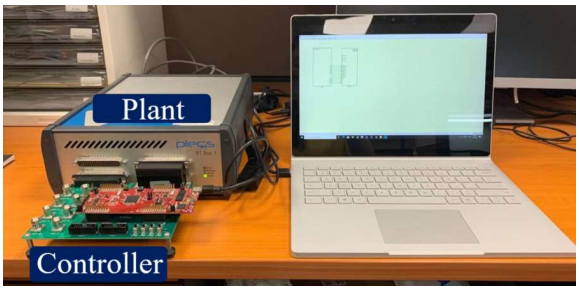

Fig. 31. HIL Platform photo of the mechanical system.

The well-known rotor flux field-oriented control (RFOC) is implemented in this paper to independently control the flux-producing current and torque-producing current [33]–[34]. To be more specific, the d-axis current is controlled to maintain the desired rotor flux λ_{r_ref} and the q-axis current is controlled to achieve the expected electromagnetic torque reference.

To actively damp the torsional vibrations, the speed difference is utilized as feedback and the principle behind has already been demonstrated in Fig. 13(a). Notice that the shaft torque derivative feedback in Fig. 13(b) can also achieve an equivalent effect. All the system and control parameters are extensively provided in Table III.

Fig. 32 displays the HIL results without the active damping. The speed of the induction motor is regulated to be1200 rpm to maintain the normal operation. Disturbances are created by increasing the load torque from 0 N·m to 30 N·m when $t = t_1$ and decreasing the load torque from 30 N·m to 0 N·m when $t = t_2$. It can be observed that the motor speed and load speed suffer from oscillations during the transient stage. In addition to this, the torsional vibrations are much severe for the shaft torque T_{sh}, which would greatly compromise the lifetime of a mechanical system.

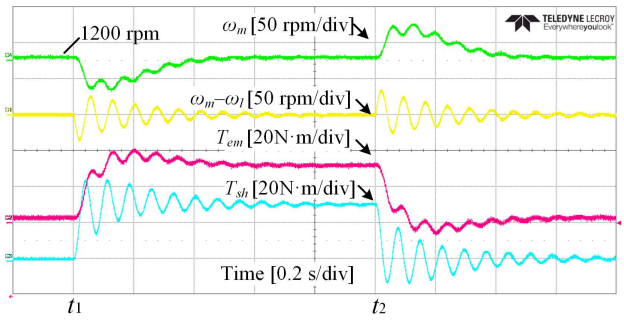

Fig. 32. HIL test results without the active damping control.

This article has been accepted for publication in a future issue of this journal, but has not been fully edited. Content may change prior to final publication. Citation information: DOI 10.1109/TIE.2021.3095796, IEEE Transactions on Industrial Electronics

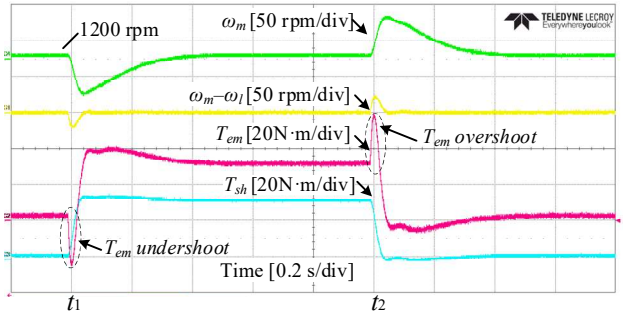

Fig. 33. HIL test results with the active damping control. (K=15)

In comparison, Fig. 33 shows the HIL test results using the active damping, i.e., speed difference feedback control. It is clearly observed that the motor angular speed ω_m as well as the load mass speed ω_l can smoothly transit to the new equilibrium points after the step load torque change. In the meantime, torsional vibrations are effectively mitigated so that the shaft torque T_{sh} is free from low-frequency oscillation. A comparison between Fig. 32 and Fig. 33 implies that torsional vibrations may not be effectively addressed by the speed control loop, but can be well suppressed if the active damping term, like the speed difference feedback and shaft torque derivative feedback, is incorporated into the outer-loop of the motor drive controller. Based on the parameters in Table IV, and damping coefficient ζ is calculated to be 0.433. Substitute ζ into (35), the peak value of T_{em_ad} is calculated to be 30.3N.m. The measured electromagnetic torque T_{em} peak value is 30N.m+25.2N.m =55.2N.m during the load step decrease event. The additional 25.2N.m electromagnetic torque is mainly contributed by fast increasing of T_{em_ad} but also affected by the slow decreasing of T_{ref} as analyzed in section IV.

VI. Conclusion

This paper analyzes and derives the mathematical models of the electrical *LCL* system and the mechanical *JKJ* system. It is revealed that the variables in the electrical system can be linked with the variables in the mechanical system through one-to-one mappings. This theoretical finding implies that the plant models, open- and closed-loop transfer functions, and active damping schemes are fundamentally the same for both the electrical and mechanical systems. Two examples namely capacitor current feedback based active damping for *LCL* system and speed difference based active damping for *JKJ* system are investigated to verify the findings. Due to the high similarity, it is envisioned that the active damping algorithms in the electrical or mechanical field can be unified and mutually shared. Researchers working in either electrical or mechanical area are encouraged to review achievements in both areas to have wider scope of prior-arts in mind and avoid reinventing the wheel before trying to explore new control algorithms in future. Another finding to highlight is the substantial electromagnetic torque overshoot was introduced when performing torsional vibration suppression control during step load decrease event. The electromagnetic torque overshoot peak value was also calculated at various damping coefficients to determine inverter current rating requirement and guide inverter design.

Acknowledgement

This work was supported by Micro Electronics R&D center of Shenzhen Topband Co., Ltd under Grant number 40121065.

References

[1] M. Liserre, F. Blaabjerg, and S. Hansen, "Design and control of an LCL filter based three-phase active rectifier," *IEEE Trans. Ind. Appl.*, vol. 41, no. 5, pp. 1281–1291, Sep./Oct. 2005.

[2] Y. Tang, P. C. Loh, P. Wang, F. H. Choo, and F. Gao, "Exploring Inherent Damping Characteristic of LCL-Filters for Three-Phase Grid-Connected Voltage Source Inverters," *IEEE Trans. Power Electron.*, vol. 27, no. 3, pp. 1433-1443, March 2012.

[3] Y. Tang, P. C. Loh, P. Wang, F. H. Choo, F. Gao, and F. Blaabjerg, "Generalized design of high performance shunt active power filter with output LCL filter," *IEEE Trans. Ind. Electron.*, vol. 59, no. 3, pp. 1443–1452, Mar. 2012.

[4] R. Pena-Alzola, M. Liserre, F. Blaabjerg, R. Sebastian, J. Dannehl, and F. W. Fuchs, "Analysis of the passive damping losses in LCL-filter based grid converters," *IEEE Trans. Power Electron.*, vol. 28, no. 6, pp. 2642–2646, Jun. 2013.

[5] S.G. Parker, B. P. McGrath, and D. G. Holmes, "Regions of active damping control for LCL filters," *IEEE Trans. Ind. Appl.*, vol. 50, no. 1, pp. 424–432, Jan./Feb. 2014.

[6] M. Wagner, T. Barth et. al, "Discrete-Time Active Damping of LCL-Resonance by Proportional Capacitor Current Feedback", *IEEE Trans. Ind. Appl.,* vol. 50, no. 6, pp. 3911–3920, Nov./Dec. 2014.

[7] X. Wang, F. Blaabjerg, and P. C. Loh, "Virtual RC damping of LCL filtered voltage source converters with extended selective harmonic compensation," *IEEE Trans. Power Electron.*, vol. 30, no. 9, pp. 4726–4737, Sep. 2015.

[8] J. Dannehl, F. W. Fuchs, S. Hansen, and P. B. Thogersen, "Investigation of active damping approaches for PI-based current control of grid-connected pulse width modulation converters with LCL filters," *IEEE Trans. Ind. Appl*., vol. 46, no. 4, pp. 1509–1517, Jul./Aug. 2010.

[9] J. He and Y. W. Li, "Generalized Closed-Loop Control Schemes with Embedded Virtual Impedances for Voltage Source Converters with LC or LCL Filters," *IEEE Trans. Power Electron*., vol. 27, no. 4, pp. 1850-1861, April 2012.

[10] Y. Jia, J. Zhao and X. Fu, "Direct Grid Current Control of LCL-Filtered Grid-Connected Inverter Mitigating Grid Voltage Disturbance," *IEEE Trans. Power Electron*., vol. 29, no. 3, pp. 1532-1541, March 2014.

[11] Z. Xin, P. C. Loh, X. Wang, F. Blaabjerg, and Y. Tang, "Highly Accurate Derivatives for LCL-Filtered Grid Converter With Capacitor Voltage Active Damping", *IEEE Trans. Power Electron*., vol. 31, no. 5, pp. 3612–3625, May. 2016.

[12] Z. Xin, X. Wang, P. C. Loh, and F. Blaabjerg, "Realization of digital differentiator using generalized integrator for power converters," *IEEE Trans. Power Electron*., vol. 30, no. 12, pp. 6520-6523, Dec. 2015.

[13] W. Yao, Y. Yang, X. Zhang and F. Blaabjerg, "Digital notch filter based active damping for LCL filters," 2015 *IEEE Applied Power Electronics Conference and Exposition* (APEC), pp. 2399-2406, 2015.

[14] J. Dannehl, M. Liserre, and F. W. Fuchs, "Filter-Based Active Damping of Voltage Source Converters With LCL Filter", *IEEE Trans. Ind. Electron*., vol. 58, no. 8, pp. 3623-3633, Aug. 2011.

[15] W. Yao, Y. Yang, X. Zhang, F. Blaabjerg, and P. C. Loh, "Design and Analysis of Robust Active Damping for LCL Filters Using Digital Notch Filters", *IEEE Trans. Power Electron*., vol. 32, no. 3, pp. 2360–2375, Mar. 2017.

[16] R. Peña-Alzola, M. Liserre, F. Blaabjerg, M. Ordonez, and T. Kerekes, "A Self-commissioning Notch Filter for Active Damping in a Three-Phase LCL -Filter-Based Grid-Tie Converter," *IEEE Trans. Power Electron*., vol. 29, no. 12, pp. 6754-6761, Dec. 2014.

[17] G. Shen, X. Zhu, J. Zhang. and D. Xu, "A New Feedback Method for PR Current Control of LCL-Filter-Based Grid-Connected Inverter," *IEEE Trans. Ind. Electron.*, vol. 57, no. 6, pp. 2033-2041, June 2010.

[18] Z. Gao, S. Hu, and F. Jiang, "A novel motion control design approach based on active disturbance rejection," *Proceedings of the* 40th *IEEE Conference on Decision and Control* (Cat. No.01CH37228), pp. 4877-4882, vol. 5, 2001.

[19] A. Benrabah, D. Xu and Z. Gao, "Active Disturbance Rejection Control of LCL-Filtered Grid-Connected Inverter Using Padé Approximation," *IEEE Trans. Ind. Appl*., vol. 54, no. 6, pp. 6179-6189, Nov.-Dec. 2018.

[20] G. Mandic, A. Nasiri, E. Muljadi, and F. Oyague, "Active Torque Control for Gearbox Load Reduction in a Variable-Speed Wind Turbine", *IEEE Trans. Ind. Appl.*, vol. 48, no. 6, pp. 2424-2432, Dec. 2012
[21] K. Sugiura and Y. Hori, "Vibration suppression in 2- and 3-mass system based on the feedback of imperfect derivative of the estimated torsional torque," *IEEE Trans. Ind. Electron*., vol. 43, no. 2, pp. 56–64, Apr. 1996.
[22] J. K. Ji, and S. K. Sul, "Kalman Filter and LQ Based Speed Controller for Torsional Vibration Suppression in a 2-Mass Motor Drive System", *IEEE Trans. Ind. Electron*., vol. 42, no. 6, pp. 564–571, Dec. 1995.
[23] T. O. Kowalska, and K. Szabat, "Damping of Torsional Vibrations in Two-Mass System Using Adaptive Sliding Neuro-Fuzzy Approach", *IEEE Trans. Ind. Electron*., vol. 4, no. 1, pp. 47-57, Feb. 2008.
[24] T. O. Kowalska, and M. Kaminski, "FPGA Implementation of the Multilayer Neural Network for the Speed Estimation of the Two-Mass Drive System", *IEEE Trans. Ind. Informat*., vol. 7, no. 3, pp. 436-445, Aug. 2011.
[25] K. Szabat, and T. O. Kowalska, "Vibration Suppression in a Two-Mass Drive System Using PI Speed Controller and Additional Feedbacks—Comparative Study", *IEEE Trans. Ind. Electron*., vol. 54, no. 2, pp. 1193-1206, Apr. 2007
[26] J. K. Kambrath, C. Yoon, X. Liu, Y. Wang, Y. J. Yoon, C. J. Gajanayake, and A. K. Gupta, "Direct Drive Propeller System Modelling and Active Protection", *IEEE Energy Conversion Congress and Exposition* (ECCE 2018), pp. 3901-3908, Portland, Oregon, USA, 2018.
[27] J. K. Kambrath, C. Yoon, J. Mathew, X. Liu, Y. Wang, C. J. Gajanayake, A. K. Gupta, and Y. J. Yoon, "Mitigation of Resonance Vibration Effects in Marine Propulsion", *IEEE Trans. Ind. Electron*., vol. 66, no. 8, pp. 6159-6169, Aug. 2019.
[28] J. K. Kambrath, Y. Wang, Y. J. Yoon, A. A. Ayu, X. Liu, G. Wilson, C. J. Gajanayake, and A. K. Gupta, "Modeling and Control of Marine Diesel Generator System With Active Protection", *IEEE Transactions on Transportation Electrification*, vol. 4, no. 1, pp. 249-271, Mar. 2018.
[29] J. M. Pacas, J. Armin, and T. Eutebach, "Automatic identification and damping of torsional vibrations in high-dynamic-drives," in Proc. ISIE, Cholula-Puebla, Mexico, pp. 201–206, 2000.
[30] Y. Chen, M. Yang, J. Long, K. Hu, D. Xu, and F. Blaabjerg, "Analysis of Oscillation Frequency Deviation in Elastic Coupling Digital Drive System and Robust Notch Filter Strategy," *IEEE Trans. Ind. Electron*., vol. 66, no. 1, pp. 90-101, Jan. 2019.
[31] D.-H. Lee, J. H. Lee, and J.-W. Ahn, "Mechanical vibration reduction control of two-mass permanent magnet synchronous motor using adaptive notch filter with fast Fourier transform analysis," *IET Electr. Power Appl*., vol. 6, no. 7, pp. 455–461, Aug. 2012.
[32] S. Zhao and Z. Gao, "An active disturbance rejection based approach to vibration suppression in two-inertia systems," *Proceedings of the 2010 American Control Conference*, pp. 1520-1525, 2010.
[33] J. K. Kambrath, M. S. U. Khan, Y. Wang, A. I Maswood, Y. J. Yoon, "A Novel Control Technique to Reduce the Effects of Torsional Interaction in Wind Turbine System", *IEEE Journal of Emerging and Selected Topics in Power Electronics*, vol. 7, no. 3, pp. 2090-2105, Sep. 2019.
[34] D. Telford, M. W. Dunnigan, and B. W. Williams, "Online identification of induction machine electrical parameters for vector control loop tuning," *IEEE Trans. Ind. Electron.*, vol. 50, no. 2, pp. 253–261, Apr. 20.

Xiong Liu (S'09–M'14–SM'19) received the B.E. and M.Sc. degrees in electrical engineering from Huazhong University of Science and Technology, Wuhan, China, in 2006 and 2008, respectively, and the Ph.D. degree from the School of Electrical and Electronic Engineering, Nanyang Technological University, Singapore in 2013.

From July to November 2008, he was an Engineer with Shenzhen Nanrui Technologies Company Ltd., Shenzhen, China. From September 2011 to January 2012, he was a Visiting Scholar with the Department of Energy Technology, Aalborg University, Aalborg East, Denmark. From April 2012 to December 2013, he was a Researcher with the Energy Research Institute, Nanyang Technological University. From December 2013 to July 2020, He was working as a Principal Technologist in Rolls-Royce Electrical, Rolls-Royce Singapore Pte. Ltd., Singapore. He is currently an Associate Professor with the Energy Electricity Research Center, International Energy College, Jinan University, Zhuhai, China. His research interests include power electronics, motor drive, and electrical/hybrid propulsion system for marine and aerospace.

Dr. Liu was the recipient of the Best Paper Award at the IEEE International Power Electronics and Motion Control Conference-Energy Conversion Congress and Exposition Asia in 2012.

Yang Qi (S'17) received the B.Sc. degree in electrical engineering from Xi'an Jiaotong University, China, in 2016. He was a visiting student with the Power Electronics, Microgrids, and Subsea Electrical Systems Center in 2019. He received the Ph. D. degree from Nanyang Technological University in 2021.

Since March 2021, he has been with the School of Automation, Northwestern Polytechnical University as an Associate Professor. His research interests include modeling, analysis, and control of power-electronics-based power systems.

Yi Tang (S'10-M'14-SM'18) received the B.Eng. degree in electrical engineering from Wuhan University, Wuhan, China, in 2007 and the M.Sc. and Ph.D. degrees from the School of Electrical and Electronic Engineering, Nanyang Technological University, Singapore, in 2008 and 2011, respectively. From 2011 to 2013, he was a Senior Application Engineer with Infineon Technologies Asia Pacific, Singapore. From 2013 to 2015, he was a Postdoctoral Research Fellow with Aalborg University, Aalborg, Denmark. Since March 2015, he has been with Nanyang Technological University, Singapore, where he is currently an Associate Professor. He is the Cluster Director of the Advanced Power Electronics Research Program at the Energy Research Institute, Nanyang Technological University.

Dr. Tang was a recipient of the Infineon Top Inventor Award in 2012, the Early Career Teaching Excellence Award in 2017, the Best Associate Editor Award for IEEE Jounral of Emerging and Selected Topics in Power Electronics in 2018, the Outstanding Reviewer for the IEEE Transactions on Power Electronics in 2019, and four IEEE Prize Paper Awards. He is an Associate Editor for the IEEE Transactions on Power Electronics and the IEEE Jounral of Emerging and Selected Topics in Power Electronics.

Yuanpeng Guan received the B.S. degree in electrical engineering from the Huazhong University of Science and Technology, Wuhan, China, in 2014, the M.S. degree in power electronic from South China University of Technology, Guangzhou, China, in 2017, and the Ph.D. degree in power electronic from the School of Electric Power, South China University of Technology, Guangzhou, China, in 2020. He is currently an Associate Professor at the Energy Electricity Research Center, International Energy College, Jinan University, Zhuhai, Guangdong, China. His current research interests include grid-connected inverter and dual-active-bridge dc-dc converter.

Peng Wang (Fellow, IEEE) received the B.Sc. degree in electrical engineering from Xi'an Jiaotong University, Xi'an, China, in 1978, the M.Sc. degree in electrical engineering from the Taiyuan University of Technology, Taiyuan, China, in 1987, and the M.Sc. and Ph.D. degrees in electrical engineering from the University of Saskatchewan, Saskatoon, SK, Canada, in 1995 and 1998, respectively. He is currently a Professor of electrical engineering with Nanyang Technological University, Singapore.

Frede Blaabjerg (S'86–M'88–SM'97–F'03) was with ABB-Scandia, Randers, Denmark, from 1987 to 1988. From 1988 to 1992, he got the PhD degree in Electrical Engineering at Aalborg University in 1995. He became an Assistant Professor in 1992, an Associate Professor in 1996, and a Full Professor of power electronics and drives in 1998. From 2017 he became a Villum Investigator. He is honoris causa at University Politehnica Timisoara (UPT), Romania and Tallinn Technical University (TTU) in Estonia.
His current research interests include power electronics and its applications such as in wind turbines, PV systems, reliability, harmonics and adjustable speed drives. He has published more than 600 journal papers in the fields of power electronics and its applications. He is the co-author of four monographs and editor of ten books in power electronics and its applications.
He has received 33 IEEE Prize Paper Awards, the IEEE PELS Distinguished Service Award in 2009, the EPE-PEMC Council Award in 2010, the IEEE William E. Newell Power Electronics Award 2014, the Villum Kann Rasmussen Research Award 2014, the Global Energy Prize in 2019 and the 2020 IEEE Edison Medal. He was the Editor-in-Chief of the IEEE TRANSACTIONS ON POWER ELECTRONICS from 2006 to 2012. He has been Distinguished Lecturer for the IEEE Power Electronics Society from 2005 to 2007 and for the IEEE Industry Applications Society from 2010 to 2011 as well as 2017 to 2018. In 2019-2020 he served as a President of IEEE Power Electronics Society. He has been Vice-President of the Danish Academy of Technical Sciences. He is nominated in 2014-2020 by Thomson Reuters to be between the most 250 cited researchers in Engineering in the world.